Preprint
UCRL-JC-148864

Modeling of Thermal Convection of Liquid TNT for Cookoff

R. McCallen, T. Dunn, A. Nichols, J. Reaugh, M. McClelland

This article was submitted to
Nuclear Explosives Code Development Conference, Monterey, CA, October 21-24, 2002

February 27, 2003

This work was performed under the auspices of the United States Department of Energy by the University of California, Lawrence Livermore National Laboratory under contract No. W-7405-Eng-48.

Proceedings of the NECDC 2002

Modeling of Thermal Convection of Liquid TNT for Cookoff(U)

Rose McCallen, Timothy Dunn, Albert Nichols, Jack Reaugh, Matthew McClelland

Lawrence Livermore National Laboratory, Livermore, CA 94551

The objective is to computationally model thermal convection of liquid TNT in a heated cylindrical container for what are called 'cookoff' experiments. Our goal is to capture the thermal convection coupled to the heat transfer in the surrounding container. We will present computational results that validate the functionality of the model, numerical strategy, and computer code for a model problem with Rayleigh number of $O(10^6)$. We solve the problem of thermal convection between two parallel plates in this turbulent flow regime and show that the three-dimensional computations are in excellent agreement with experiment. (U)

Background

The objective is to computationally model thermal convection of liquid TNT in a heated cylindrical container. This effort is motivated by the need to expand our understanding of when and how TNT initiates from relatively slow heating. The laboratory experiments used to investigate initiation and level of reactive violence are called 'cookoff' experiments. Cookoff experiments provide scientists and engineers the time to initiation and the energetic level of an explosion due to the heating of an explosive. However, experiments are expensive and provide a limited amount of information. The capability to computationally model cookoff experiments is needed to improve the design and data acquisition for the experiments, reduce the number of experiments, investigate scenarios that are difficult to experimentally study, and improve the understanding of the physics phenomena.

The work presented here focuses on the case of melted TNT. Past work uses an effective conductivity to approximate the thermally driven convection in the cylinder for fully melted TNT. Our goal is to capture the thermal convection coupled to the heat transfer in the surrounding container. We will present computational results that verify the functionality of the model for this application, and more specifically, for the applicable range of Rayleigh number. Rayleigh number (*Ra*) is a dimensionless number that represents the level of buoyancy driven convection.

A typical scaled thermal explosion experiment (STEX) (*Wardell and Meinshein, 19XX*) involves the 'cookoff' cylinder containing the explosive, in a partially open box to capture shrapnel, which is placed inside a vessel to fully contain the explosion. A schematic of this setup indicating the heating and flow mechanisms is shown in Figure 1. Table 1 provides the non-dimensional parameters of interest for liquid TNT. The Peclet

numbers (*Pe*) for thermal and mass transport are very large and mass diffusion is 100 times larger than thermal diffusion. Thus, for liquid TNT in cookoff experiments, thermal transport by convection is expected to be much greater than thermal transport by conduction.

The predicted *Ra* for the liquid TNT case is in the unstable turbulent regime, which poses a physics modeling and computational challenge. Parmetier and Sotin (2000) generated and evaluated three-dimensional (3D) direct numerical simulations (DNS) of a thermally heated chamber for *Ra* of 10^7. Their results indicate complex flows exhibiting plumes of heated fluid that form and penetrate through regions of colder fluid. It is believed that the parametric values in Table 1 represent an upper bound and Ra is more likely to have magnitudes in the range of 10^6 to 10^7, which are still in the fully turbulent regime.

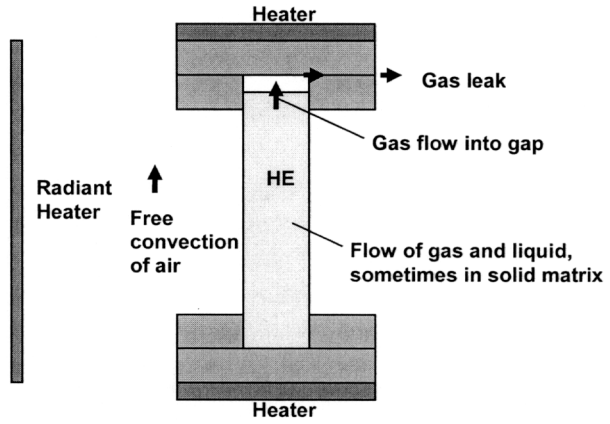

Fig. 1. The STEX experiments involve the 'cookoff' cylinder, within a partially open box, and within a vessel.

In this paper, we present comparisons of our simulations to published experimental results for code and model validation. The experimental case chosen for this investigation are those of Betts and Bokhari (2000). The basis for this selection was the simplicity of the geometry, the relevance of the *Ra* case tested (*Ra* = 1.43 x 10^6) to the "cookoff" problem of interest, and the availability of the experimental data which is provided on a website (http://cfd.me.umist.ac.uk /cgi-bin/cfddb).

Table 1. Upper parameter levels for pure liquid flow conditions.

	Pure TNT (water like liquid)
$\Delta T_o C$	**10**
V_s**(cm/s), liquid velocity scale**	**4**
L_s **(cm), cylinder diameter**	**5.08**
$t_s = L_s / V_s$	**1.3 s**
Pe(thermal)=RePr (Pr=$c_p\mu/k$**)**	**10,000**
Pe(mass)=ScPr	**1x10^6**
$Re=V_sL_s/\nu$	**13,000**
$Gr=g\beta\rho^2L_s^3\Delta T/\mu^2$	**2x10^8**
$Ra=GrPr= g\beta\rho c_pL_s^3\Delta T/k\nu$	**3x10^8**

This is a work in progress

report and future efforts are identified.

Problem Definition

The following subsections describe the experimental setup and the computational model definition.

Experimental Setup and Data

The experimental setup is a 3D box with top and bottom rubber insulation and constant temperature side walls set so that *Ra* based on the cavity width is 1.43 x 10^6 (Figure 2) (*Betts and Bokhari, 2000*). The height to width of the channel is $H/W = 28.7$ and the depth to width is $D/W = 6.8$. The hot wall is maintained at 327.7K and the cold wall at 288.6K.

The tall yet skinny channel with a substantial depth was chosen to ensure turbulent flow characteristics would be exhibited (i.e., 3D, random like, with a wide range of scales).

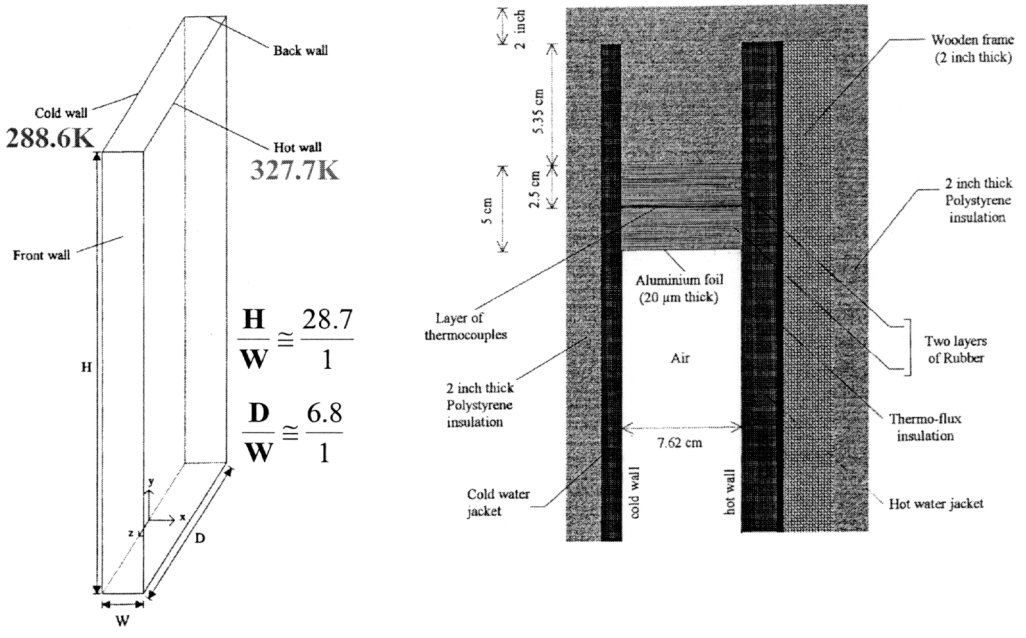

Betts and Bokhari., Inter. Journal of Heat and Fluid Flow 21(2000) 675-683

Fig. 2. The experimental setup is a 3D box with top and bottom rubber insulation and constant temperature side walls.

The rubber stops were used to obtain a well defined thermal boundary condition on the unheated walls (i.e., linearly varying temperature).

The experimental fluid is dry air. The Prandtl number (*Pr*) for dry air is approximately 0.7 and *Pr* for liquid TNT is roughly 0.7, so results should be comparable.

Computational Model Setup

The computational model is a 3D slice of the experimental geometry (Figure 3) including the rubber stops at the top and bottom. The depth of the slice is the same as the width for the simulations reported in this paper. The hot and cold walls are treated as temperature

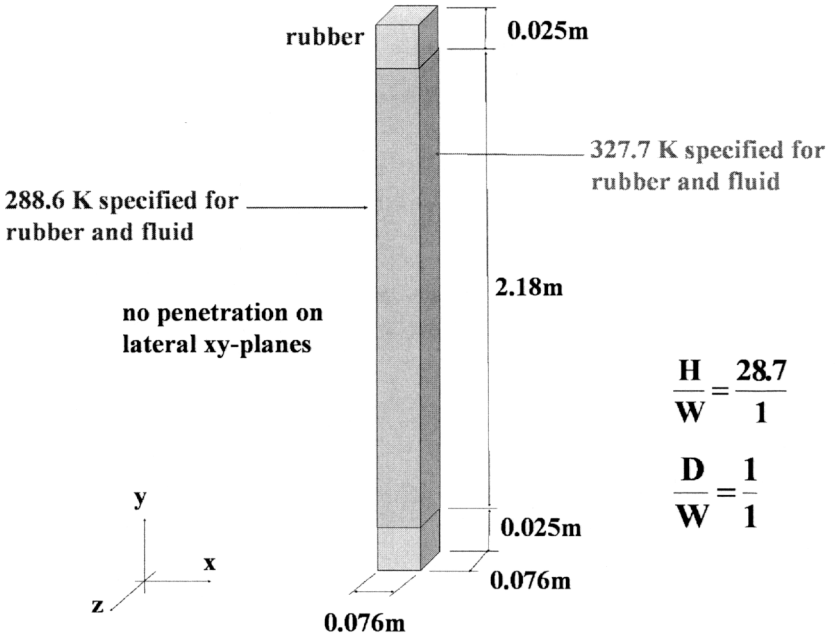

Fig. 3. The computational model is a 3D slice of the experimental geometry.

boundary conditions and no slip walls for the flow boundary conditions. The lateral *x-y* planes are specified as no penetration flow boundary conditions and insulated heat transfer boundary conditions. No slip flow conditions are specified on the interfacing wall between the fluid and rubber stops. The rubber stops have similar heat transfer boundary conditions with temperature boundary conditions for the *z-y* planes and insulated boundary conditions for the *x-y* planes, as well as the external bounding *x-z* planes. The computational elements in the rubber material are designated as non-fluid elements and flow computations are not performed in these regions.

A fine and a coarse grid solution were generated. Both grids have 3 elements in the height of each rubber stop. The fluid elements alone included 45x450x15 elements for the fine grid and 30x300x10 elements for the coarse grid, respectively in the *x, y,* and *z* directions. The total number of elements including the rubber stops is 307,800 for the fine grid and 91,800 for the coarse grid. The fluid grids are graded towards the wall with a grading ratio of 3:1 in the *x*-direction and 4:1 in the *y*-direction from the center of the cavity to the wall for both grids. The grid is uniformly spaced in the z-direction.

The material properties used in the simulations for the fluid are those specified in Betts and Bokhari, 2000 for dry air. Whether to use the heat capacity for constant pressure or

constant volume for the heat transfer model is not a straight forward choice (see for example, *Panton, 1984*). For the calculations herein, the heat capacity for constant volume, c_v, is used for the fluid elements.

Computational Approach

The incompressible flow solver is coupled with the thermal diffusion model in the flow regions by operator splitting. More specifically, the temperature is solved independent of the flow equations, but are coupled through the temperature-advection term in the heat transfer model and a Bousinessq term in the incompressible flow model to capture thermal buoyancy effects.

Flow Solution

The continuum equations that are being used to model the flow are the time-dependent 3D incompressible Navier Stokes equations

$$\frac{\partial u_\alpha}{\partial x_\alpha} = 0$$

$$\frac{\partial u_\alpha}{\partial t} + u_\beta \frac{\partial u_\alpha}{\partial x_\beta} = \frac{\partial \tau_{\alpha\beta}}{\partial x_\beta}$$

where

$$\tau_{\alpha\beta} = -\frac{p}{\rho}\delta_{\alpha\beta} + \nu \frac{\partial u_\alpha}{\partial x_\beta}$$

u_α is the velocity, p is the pressure and, ρ is the density.

An Eulerian formulation of the equations is solved using a Galerkin finite element method (FEM). The method is described in detail in Gresho and Sani (1998). The discretized continuity and momentum equations can be written in matrix form as

$$\boldsymbol{C}^T \boldsymbol{u} = 0$$

$$\boldsymbol{M}\dot{\boldsymbol{u}} + [\boldsymbol{K} + \boldsymbol{N}(u)]\boldsymbol{u} + \boldsymbol{CP} = \boldsymbol{F}$$

where $\boldsymbol{u}$ is the velocity vector, $\boldsymbol{P}$ is the pressure vector (p/ρ), $\boldsymbol{M}$ is the mass matrix, $\boldsymbol{K}$ is the diffusivity, $\boldsymbol{N(u)}$ is the advection operator, $\boldsymbol{C}$ is the gradient operator, and $\boldsymbol{F}$ is the user

supplied natural boundary condition. With the centroid advection velocity approximation, we have

$$\boldsymbol{C} = -\int_{\Omega} \psi_n \frac{\partial \phi_i}{\partial x_\alpha}, \quad \boldsymbol{M} = \int_{\Omega} \phi_i \phi_j, \quad \boldsymbol{K} = \int_{\Omega} \nu \frac{\partial \phi_i}{\partial x_\beta} \frac{\partial \phi_j}{\partial x_\beta}, \quad \boldsymbol{N}(u) = u_\beta^k \int_{\Omega} \phi_i \phi_k \frac{\partial \phi_j}{\partial x_\beta},$$
$$\boldsymbol{f} = \int_{\partial\Omega} \phi_i f_\alpha + \boldsymbol{f_B}$$

where

$$f_\alpha = n_\beta(-P\delta_{\alpha\beta} + \nu \frac{\partial u_\alpha}{\partial x_\beta})$$

and $\boldsymbol{f_B}$ is the Boussinesq term defined below.

For this investigation the *Q1Q0* element formulation[1] was used for eight-node hexahedral brick elements. This provides linear velocity interpolation and piecewise constant pressure. The coefficient matricies were generated using full 8-point Gaussian quadrature. Balancing tensor diffusivity is added to balance the negative diffusion induced by the explicit forward-Euler time integration. Full integration of the advection term is available, but to reduce the computational effort, a 'centroid advection velocity' approximation is used in the evaluation of the advection term, as shown above in the definition of *N(u)*.

The continuity and momentum equations can be solved together for the velocity, $\boldsymbol{u}^{n+1}$, and pressure, $\boldsymbol{P}^n$, with the explicit forward-Euler time integration

$$\begin{bmatrix} \boldsymbol{M} & \boldsymbol{C} \\ \boldsymbol{C}^T & 0 \end{bmatrix} \begin{bmatrix} \boldsymbol{u}^{n+1} / \Delta t \\ \boldsymbol{P}^n \end{bmatrix} = \begin{bmatrix} \boldsymbol{F}^n \\ 0 \end{bmatrix}$$

where

$$\boldsymbol{F}^n = \boldsymbol{f}^n + (\frac{1}{\Delta t}\boldsymbol{M} - \boldsymbol{K} - \boldsymbol{N}(u^n))\boldsymbol{u}^n$$

Δt is the time step, and n is the time step level. For improved computational efficiency the pressure and velocity were decoupled by forming the Schur complement of the full system of equations resulting in an equivalent pressure Poisson equation (PPE) which is solved for pressure followed by a velocity update with the new pressure,

[1] The designation *QmQn* means that each component of the velocity is approximated by a continuous piecewise polynomial of degree *m* in each direction for a quadralateral in 2D or a hexahedra in 3D and likewise for the pressure, except that the polynomial is degree *n*.

$$\boldsymbol{C}^T \boldsymbol{M}_L^{-1} \boldsymbol{C}\boldsymbol{P}^n = \boldsymbol{C}^T \boldsymbol{M}_L{}^{-1} \boldsymbol{F}^n$$

$$\boldsymbol{u}^{n+1} = \boldsymbol{u}^n + \Delta t \boldsymbol{M}_L^{-1} (\boldsymbol{F}^n - \boldsymbol{C}\boldsymbol{P}^n)$$

where a lumped mass matrix $\boldsymbol{M}_L$ is used.

The force vector, $\boldsymbol{f}$, incorporates the Boussinesq approximation to the buoyancy term and is integrated over the element volume,

$$f_B = g(1 - \beta(T - T_o))\Omega_e$$

where g is the gravitational acceleration, β is the coefficient of thermal expansion, T_o is a reference temperature, T is the temperature, and Ω_e is the element volume.

The *Q1Q0* low-order mixed finite element is unstable and can exhibit spurious pressure modes. The solution convergence rates can be improved with matrix stabilization (*Sani, et al., 1981*). Two stabilization options available in the code are a *global* jump stabilization method, first proposed by Hughes and Franca (1987), and a *local* jump stabilization method developed by Silvester and Kechkar (1990). With both these approaches, the stabilization attempts to make the pressure more continuous by the addition of a stabilization matrix $\boldsymbol{S}$ added to the left-hand-side matrix

$$\begin{bmatrix} \boldsymbol{M} & \boldsymbol{C} \\ \boldsymbol{C}^T & \boldsymbol{S} \end{bmatrix} \begin{bmatrix} \boldsymbol{u}^{n+1} / \Delta t \\ \boldsymbol{P}^n \end{bmatrix} = \begin{bmatrix} \boldsymbol{F}^n \\ 0 \end{bmatrix}$$

where $\boldsymbol{S}$ includes a tunable parameter. For this investigation local stabilization was used. With the local stabilization method, the elements are grouped in macro elements up to 2x2x2 elements in size. At boundaries, this may not be possible and the macroelements will consist of fewer than 8 elements. The advantage of the local stabilization method over the global method is that mass conservation is now enforced over local macroelements (up to the convergence tolerance of the iterative solution of $\boldsymbol{P}$) and approximately enforced for each individual element. Global stabilization only enforces mass conservation for the entire global domain. For an example of the stabilization matrix for a 2x2x2 macroelement formed by 8 hexahedral elements see Chan and Sugiyama (1997).

The above system of equations is solved using the HYPRE parallel solver package (*Chow et al., 2000*). This provides many advanced iterative linear solvers and preconditioners designed for efficient matrix solutions on massively parallel computer systems. In particular, the solver package actually uncouples the pressure from the velocity for us by forming the Schur compliment and then solves the PPE for pressure and substitutes the pressure back into the original matrix to solve for the velocity. For the results presented

here, the PPE was solved using the conjugate gradient solver with parallel sparse approximation inverse (ParaSails) preconditioning.

The flow-field is initialized by projecting to a divergence-free velocity field. The projection is performed by enforcing the boundary conditions and solving coupled system of equations using the user-specified velocity field, $\boldsymbol{u}^0$, to calculate the right-hand-side,

$$\begin{bmatrix} \boldsymbol{M} & \boldsymbol{C} \\ \boldsymbol{C}^T & 0 \end{bmatrix} \begin{bmatrix} \boldsymbol{u}^0 / \Delta t \\ \boldsymbol{P}^n \end{bmatrix} = \begin{bmatrix} \boldsymbol{F}^0 \\ 0 \end{bmatrix},$$

so that the computed initial velocity field, $\boldsymbol{u}^0$, is divergence free, $\boldsymbol{C}^T \boldsymbol{u}^0 = 0$.

Heat Transfer Solution

The continuum equations that are being used to model the heat transfer are the time-dependent thermal transport equations

$$\rho c \frac{\partial T}{\partial t} + u_\alpha \frac{\partial T}{\partial x_\alpha} = \frac{\partial}{\partial x_\alpha}\left(k_\alpha \frac{\partial T}{\partial x_\alpha} \right) + Q$$

where ρ is the density, c is the heat capacitance, T is temperature, k_α is the material conductivity, and Q is a source term.

The temperature is solved independent of the flow equations using a Galerkin FEM for a fixed geometry and grid. The advection-diffusion equation is used for thermal transport and can be expressed in matrix form as

$$\boldsymbol{M}_{ad}\dot{\boldsymbol{T}} + \left(\boldsymbol{H}(T) + \boldsymbol{N}_{ad}(u)\right)\boldsymbol{T} = \boldsymbol{Q} + \boldsymbol{f}_{ad}$$

where

$$\boldsymbol{M}_{ad} = \left(\int_\Omega \phi_i \rho c \phi_j \right), \quad \boldsymbol{H}(T) = \left(\int_\Omega \frac{\partial \phi_i}{\partial x_\alpha} k_\alpha \frac{\partial \phi_j}{\partial x_\alpha} \right), \quad \boldsymbol{Q} = \int_\Omega \phi_i Q, \quad \boldsymbol{f}_{ad} = \int_{\partial\Omega} \phi_i \gamma,$$

$$\boldsymbol{N}_{ad} = \int_\Omega \rho c u_\alpha \phi_i \frac{\partial \phi_j}{\partial x_\alpha}$$

and the natural boundary condition is

$$\gamma = n_\beta k_\alpha \frac{\partial T}{\partial x_\alpha}$$

where n_β is the unit outward normal to the domain boundary, and summation over j is implied.

For this investigation trilinear temperature interpolation was used for the eight-node hexahedral brick elements. The coefficient matricies were generated using full 8-point Gaussian quadrature and the thermal transport equations are solved using an explicit time integration.

Analysis of Results

The following describes the simulation results for the course and fine grid solutions and a comparison of the computed and experimental results.

Computations

Comparison of the variation in time-averaged temperature for the coarse and fine grids is shown in Figures 4. Both grids predict similar temperature gradients at the walls and the predicted temperatures in the central region of the cavity are in close agreement The temperatures predicted at the lowest vertical location of $y/H = 0.05$ show the most variation. But even here, the magnitude of the temperature in the central region at $x =$ 0.04m differs by less than 4K. This is only a 1% temperature variation between the coarse and fine grid solutions.

Therefore, the solutions for the coarse and fine grid are shown to be similar to within a 1% or less variation in temperature prediction and thus, in the following discussions we report on only the fine grid solution.

The simulations indicate turbulent flow (i.e., 3D, random like, and a wide range of length scales) in agreement with experiment. This characteristic is shown in the instantaneous snapshot provided in Figure 5 and in the point time histories in Figure 6.

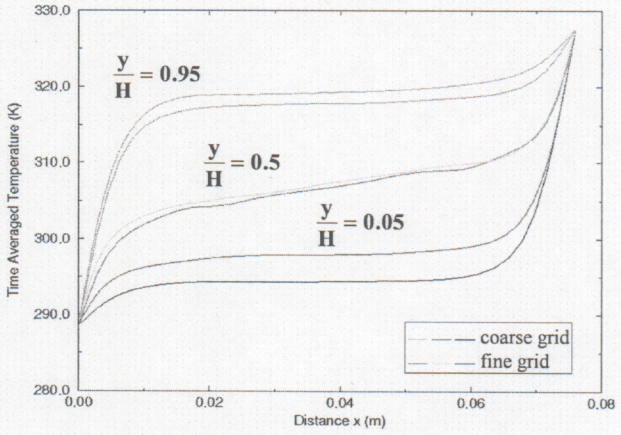

Fig. 4. Comparison of the time-averaged temperature variation with horizontal distance for the fine and coarse grid.

Because the flow field results for both the fine and coarse grids exhibit a smooth, well behaved flow field that is void of wiggles (i.e., unphysical oscillations of the velocity field from one grid to the next, indicating inadequate grid resolution), the subgrid scale (SGS) model was not turned on for these simulations. The SGS model provides a

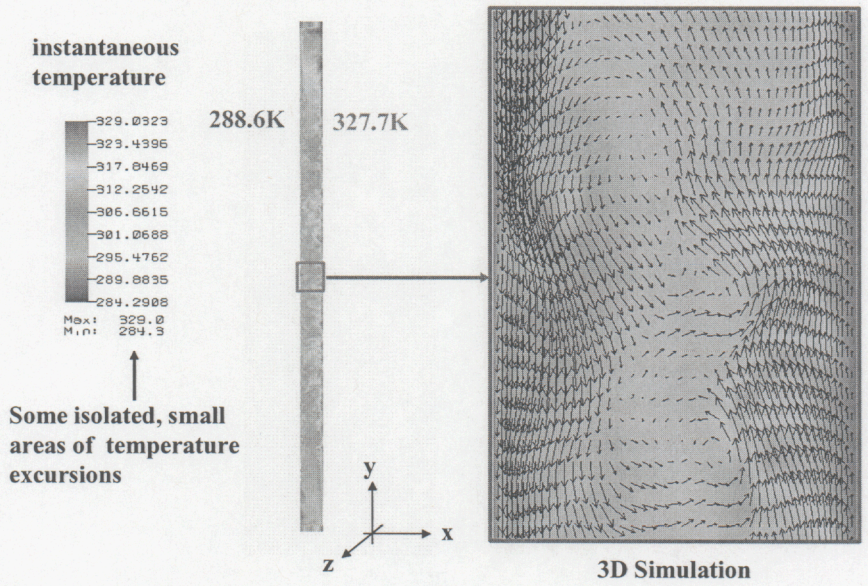

Fig. 5. Instantaneous snap shot of flow field.

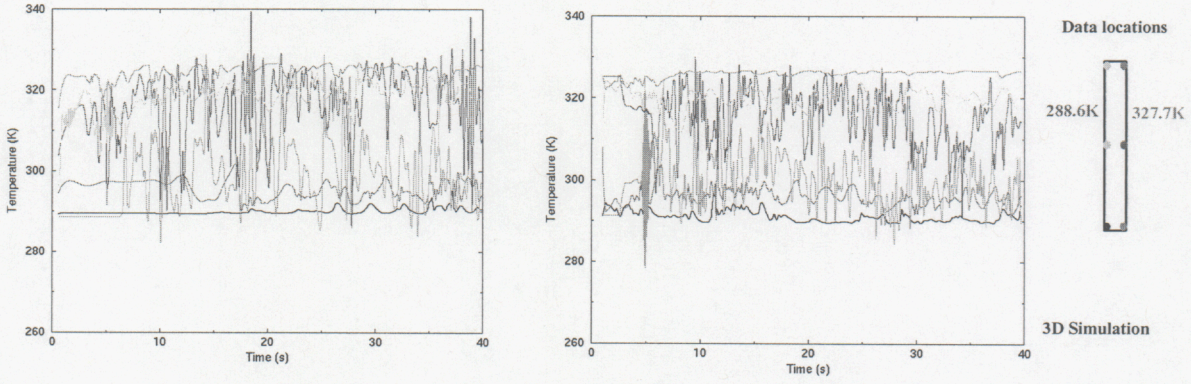

Fig. 6. Temperature time histories for the (a) coarse grid and (b) fine grid indicating random-like behavior.

turbulent eddy viscosity to approximate the eddy dissipation for the unresolved flow.[2] There are concerns that numerical dissipation is providing the needed wiggle damping and thus, behaving as the SGS model. Further investigation of this characteristic is beyond the scope of the current effort, but can be a topic of future investigations. Thus, the results reported here are the result of direct numerical simulations (DNS) without the use of an SGS model.

Another characteristic shown in Figures 5 and 6 is that the simulations exhibit some isolated, small areas of temperature excursions above the maximum wall temperature and below the minimum wall temperature. Figure 5 shows that these excursions are much more pronounced and more often for the coarse grid, compared to those for the fine grid solution. These excursions are not physical and indicate wiggles in the temperature simulation. The current code does not provide the option of a temperature SGS model, which may have been beneficial. A temperature SGS model would provide an added turbulent conduction coefficient for the unresolved temperature fluctuations. Again, further investigation of this characteristic is beyond the scope of the current effort, but can be a topic of further investigation.

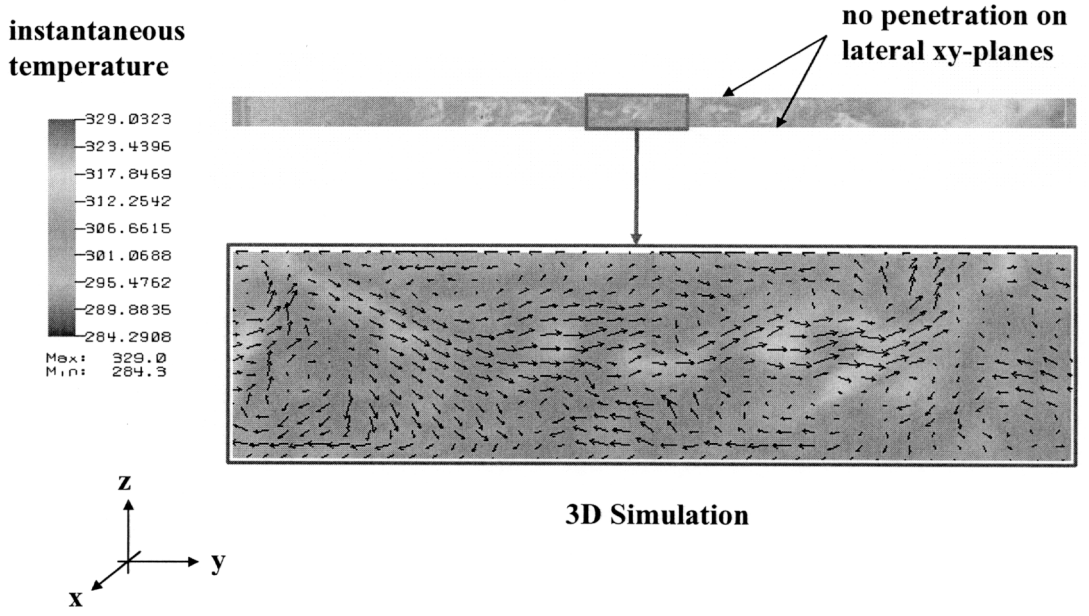

Fig. 7. Out-of-plane motion is considerable, even with the lateral boundary condition constraint.

---

[2] The flow SGS terms are

$$\partial(\upsilon_t \partial u_\alpha / \partial x_\beta) / \partial x_\beta \text{ and } \partial(\upsilon_t \partial u_\beta / \partial x_\alpha) / \partial x_\beta \text{ where } \upsilon_t$$

is defined by the magnitude of the rate of strain and the square of the grid size and an adjustable parameter (*McCallen et. al, 1997*).

Figure 7 shows that out-of-plane motion is considerable, even with the lateral flow boundary condition constraint of no penetration. Not shown are some preliminary simulations for the case of open (or natural) boundary conditions for the lateral flow condition. These laterally unbounded simulations were found to be sensitive to time step restrictions and less robust than the reported results. Future work will include investigation of the solution variation with open lateral wall flow conditions in the *xy*-plane boundaries, as well as the effect of the out-of-plane domain length.

Comparison of Simulation to Experiments

Computed time-averaged temperatures and velocities are provided on the website of experimental results and comparison to the simulations is presented below. The website also includes some transient information, but comparisons with this data will need to be a part of future studies. All comparisons of computed and experimental results described below are in reference to the fine grid solution.

Three-Dimensional Simulations

The time-averaged temperature variation with horizontal distance across the channel is compared to the experimental data at 3 height levels. As shown in Figure 8, the computed time-averaged temperatures are in very good agreement with experimentally measured time-averaged temperatures for the 3D simulations.

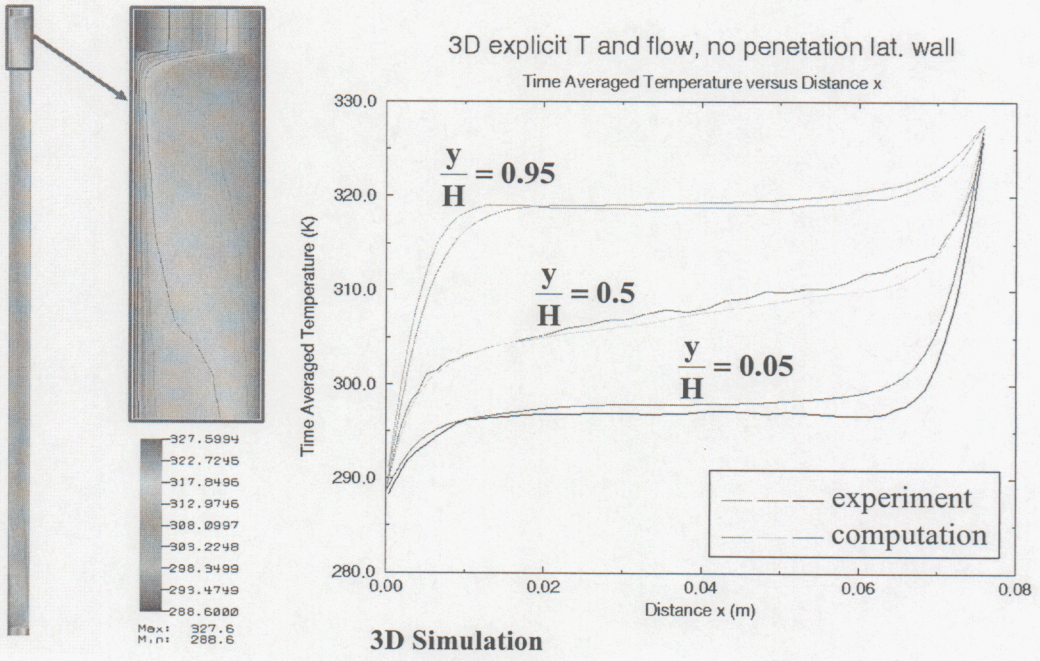

Fig. 8 Time averaged temperature compared with experiment.

Also compared are the computed and experimentally measured time-averaged vertical velocity with horizontal distance across the channel at 3 height levels. As shown in Figure 9, the computed time-averaged velocities are also in very good agreement with

experiment for the 3D simulations.

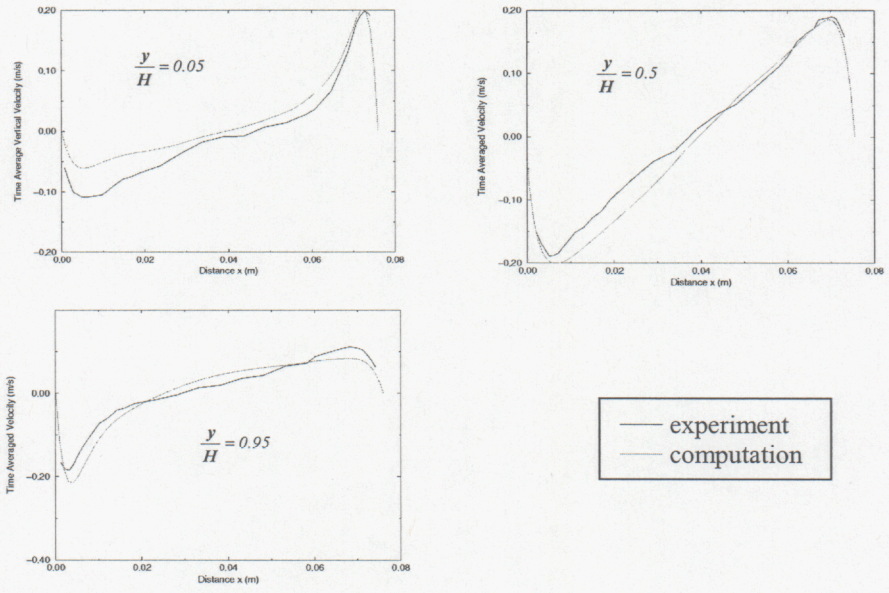

Fig. 9. Time averaged velocities compare with experiment.

Two-Dimensional Simulations

Unlike the above described 3D simulations, the 2D simulations do not accurately predict experiment. Figure 10 shows the computed and experimentally measured variation in time-averaged temperature with horizontal distance across the channel. The computed time-averaged temperature is consistently lower than the experimentally measured values.

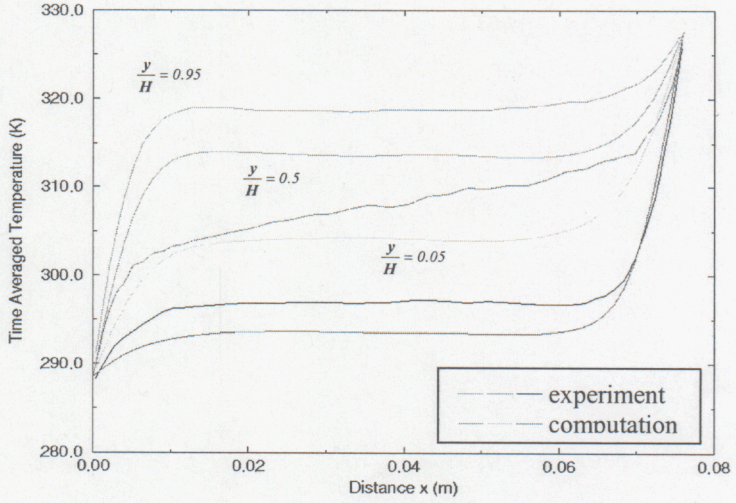

Fig. 10. The 2D simulations do not accurately predict the time-averaged experimentally measured temperatures.

Summary and Conclusions

In summary, we presented computational results that validate the functionality of the model, numerical strategy, and computer code for a model problem with Rayleigh number of $O(10^6)$. Specifically, simulations are in excellent agreement with the experiments by Betts and Bokhari, 2000 for $Ra = 1.43 \times 10^6$. Future work will include investigations of possible numerical dissipation that may be providing some local flow damping. In addition, future studies will determine the effect of open lateral wall flow conditions in the *xy*-plane boundaries, as well as the effect of the out-of-plane domain length. Finally, further analyses will include comparisons of the transient experimental data to the computations.

Acknowledgements

Work performed under the auspices of the U.S. Department of Energy by the University of California, Lawrence Livermore National Laboratory under Contract W-7405-ENG-48.

References

Betts, P.L. and Bokhari I.H., "Experiments on Turbulent Natural Convection in an Enclosed Tall Cavity," *International Journal of Heat and Fluid Flow*, **21**, 675-683 (2000).

Chan, S. T. and Sugiyama, G., *User's Manual for MC_Wind: A New Mass-Consistent Wind Model For ARAC-3*, UCRL-MA-129067, Nov. (1997).

Chow E, Cleary AJ, Falgout RD, Lambert M, Tong C, Walker D, Yang UM, *HYPRE, High Performance Preconditioners: User's Manual,* v.1.2.0 Technical Report UCRL-MA-137115-DR, Lawrence Livermore National Laboratory, CA, August (2000).

Gresho, P.M. and Sani, R.L., *Incompressible Flow and the Finite Element Method*, (John Wiley & Sons, 1998).

Hughes, T.J.R. and Franca, L.P., "A New Finite Element Formulation for Computational Fluid Dynamics: VII. The Stokes Problem with Various Well-Posed Boundary Conditions: Symmetric Formulations that Converge for All Velocity/Pressure Spaces," *Computer Method in Applied Mechanics and Engineering*, **65**, 85-96 (1987).

McCallen, R.C., Kornblum, B.T., Kollmann, W., "Large-Eddy Simulation in Complex Domains using the Finite Element Method," 1997 ASME Fluids Engineering Division Summer Meeting, FEDSM97-3496.DOC, June 22-26, (1997).

Panton R., *Incompressible Flow,* (John Wiley & Sons, 1984).

Parmetier, E.M. and Sotin, C., "Three-Dimensional Numerical Experiments on Thermal Convection in a Very Viscous Fluid: Implications for the Dynamics of a Thermal Boundary Layer at High Rayleigh Number," *Physics of Fluids*, 12 (3), 609-617 (2000).

Sani, R.L., Gresho, P.M., Lee, R.L., and Griffiths, D.F., "The Cause and Cure of the Spurious Pressures Generated by Certain FEM Solutions of the Incompressible Navier-Stokes Equations: Part 1," *International Journal for Numerical Methods in Fluids* **1,** 17-43 (1981).

Silvester, D.J. and Kechkar, N., "Stabilised Bilinear-Constant Velocity-Pressure Finite Elements for the Conjugate Gradient Solution of the Stokes Problem," *Computer Methods in Applied Mechanics and Engineering,* **79,** 71-86 (1990).

Wardell and Meinshein, 19XX